

RESEARCH ARTICLE

10.1002/2017JB014579

Key Points:

- Phase relations in the system $\text{MgSiO}_3\text{-Al}_2\text{O}_3$ were determined at temperatures up to 2300 K and pressures up to 45 GPa
- The solubility of Al_2O_3 in bridgmanite and that of MgSiO_3 in corundum increases with increasing temperature
- The Al_2O_3 cannot be fully accommodated in the coldest parts of subducted slabs in the shallow part of the lower mantle

Supporting Information:

- Supporting Information S1

Correspondence to:

Z. Liu,
bt303897@uni-bayreuth.de

Citation:

Liu, Z., Nishi, M., Ishii, T., Fei, H., Miyajima, N., Ballaran, T. B., ... Katsura, T. (2017). Phase relations in the system $\text{MgSiO}_3\text{-Al}_2\text{O}_3$ up to 2300 K at lower mantle pressures. *Journal of Geophysical Research: Solid Earth*, 122, 7775–7788. <https://doi.org/10.1002/2017JB014579>

Received 22 JUN 2017

Accepted 1 OCT 2017

Accepted article online 9 OCT 2017

Published online 26 OCT 2017

Phase Relations in the System $\text{MgSiO}_3\text{-Al}_2\text{O}_3$ up to 2300 K at Lower Mantle Pressures

Zhaodong Liu^{1,2} , Masayuki Nishi², Takayuki Ishii¹, Hongzhan Fei¹ , Nobuyoshi Miyajima¹ , Tiziana Boffa Ballaran¹ , Hiroaki Ohfuji², Takeshi Sakai², Lin Wang¹ , Svyatoslav Shcheka¹, Takeshi Arimoto², Yoshinori Tange³ , Yuji Higo³ , Tetsuo Irifune², and Tomoo Katsura¹ 

¹Bayerisches Geoinstitut, University of Bayreuth, Bayreuth, Germany, ²Geodynamics Research Center, Ehime University, Matsuyama, Japan, ³Spring-8, Japan Synchrotron Radiation Institute, Sayo, Japan

Abstract Phase relations in the system $\text{MgSiO}_3\text{-Al}_2\text{O}_3$ were investigated at pressures of 27–45 GPa and temperatures of 1700, 2000, and 2300 K using sintered diamond and tungsten carbide anvils in a multianvil apparatus. The bulk compositions in the $\text{MgSiO}_3\text{-Al}_2\text{O}_3$ binary system crystallize a phase assemblage of pyrope and corundum at pressures below 27 GPa and an assemblage of bridgmanite and corundum at pressures above 27 GPa regardless of temperatures. The solubility of Al_2O_3 in bridgmanite and that of MgSiO_3 in corundum increases significantly with increasing temperature. The solubility of Al_2O_3 in bridgmanite increases from 6.7 mol % at 1700 K to 21.8 mol % at 2500 K under a constant pressure of 27 GPa. Bridgmanite becomes more aluminous with increasing pressure from 27 to 45 GPa at a given temperature. The MgSiO_3 content in corundum increases with increasing pressure at pressure lower than 27 GPa, while it decreases at pressure higher than 27 GPa. Our results suggest that bridgmanite can incorporate a considerably higher Al_2O_3 content than that of the pyrope composition (25 mol % Al_2O_3). The present study further suggests that the entire Al_2O_3 component is accommodated into bridgmanite in the pyrolite lower mantle. However, Al_2O_3 cannot be fully accommodated into bridgmanite in the coldest parts of subducted slabs in the shallow part of the lower mantle, and therefore, additional phases such as MgAl_2O_4 with calcium ferrite-type structure are necessary to host the excess Al_2O_3 .

Plain Language Summary Here we determined the phase relations in the system $\text{MgSiO}_3\text{-Al}_2\text{O}_3$ up to 2300 K under lower mantle pressures and found that the solubility of Al_2O_3 in bridgmanite and that of MgSiO_3 in corundum increase with increasing temperature. All Al_2O_3 can be completely accommodated into bridgmanite in the pyrolite composition, while the Al_2O_3 cannot be fully accommodated into bridgmanite in the coldest parts of subducted slabs, and therefore, additional phases are required to host the excess Al_2O_3 .

1. Introduction

Al_2O_3 is the fourth most abundant component in the Earth's mantle (McDonough & Sun, 1995; Ringwood, 1975). It has been put in the spotlight because of its importance for understanding the mineralogy of the Earth's mantle. Al_2O_3 makes up about 4 wt % in the pyrolite mantle (Sun, 1982) and as much as about 16 wt % in the mid-oceanic ridge basalt (MORB) layers in subducted slabs (Green et al., 1979). From the upper mantle to the transition zone, Al_2O_3 is primarily accommodated into garnet solid solutions in both pyrolite and MORB compositions (Irifune, 1987; Ringwood, 1967). Under lower mantle conditions, the entire Al_2O_3 can be incorporated into bridgmanite, the most abundant mineral in the Earth's mantle, in the pyrolite composition (Irifune, 1994). On the other hand, bridgmanite cannot accommodate all Al_2O_3 in the MORB composition, and some Al_2O_3 may be accommodated in several Al-rich phases in addition to bridgmanite. (e.g., Hirose & Fei, 2002; Irifune & Ringwood, 1993; Ono et al., 2001). Moreover, the incorporation of Al_2O_3 can greatly change the crystal chemistry of bridgmanite (e.g., McCammon, 1997) and thereby significantly affect its physical properties such as elastic properties (Brodholt, 2000; Zhang & Weidner, 1999) and electrical conductivity (Xu et al., 1998). Therefore, knowledge about the Al_2O_3 effects on the crystal chemistry of bridgmanite is of great significance in mineral physics and geophysics and is seminal for understanding the mineralogy of the lower mantle.

To understand the Al_2O_3 solubility in bridgmanite better, phase relations in the system $\text{MgSiO}_3\text{-Al}_2\text{O}_3$ have been studied extensively at pressure below 27 GPa (Akaogi et al., 2002; Hirose et al., 2001; Irifune et al., 1996; Kubo & Akaogi, 2000). These studies suggested that bridgmanite coexists with corundum in this system

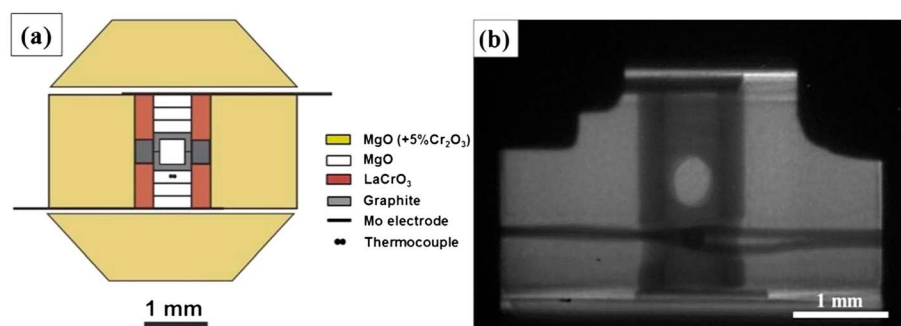


Figure 1. (a) Schematic illustration of the high-pressure cell assembly for in situ SD experiments. (b) X-ray radiographic images of SD cell assembly at ambient conditions. The hot junction of the thermocouple was placed at the bottom of the capsule, and the diffracted X-ray signals were acquired through the graphite windows.

at pressures above 26 GPa. Recently, Liu et al. (2016) demonstrated that the Al_2O_3 solubility in bridgmanite increases from 12 to 29 mol % with increasing pressure from 27 to 52 GPa at a temperature of 2000 K. The pressure dependence at a given temperature, therefore, is now clear; however, the temperature dependence of the Al_2O_3 incorporation in bridgmanite is still poorly constrained. Irifune et al. (1996) suggested that it increases from 11 mol % at 1760 K to 17 mol % at 2030 K at a pressure of 27 GPa, whereas Kubo and Akaogi (2000) experiments showed an increase from 8 to 13 mol % with increasing temperature from 1670 to 2170 K at almost the same pressure. Therefore, these two studies disagree significantly. Moreover, these studies were conducted only at the lowest-pressure conditions for the bridgmanite and corundum coexistence, and no studies have reported the temperature effect on the Al_2O_3 solubility in bridgmanite at higher pressures. Temperatures in the subducted slabs should be significantly lower than in the surrounding mantle but should approach that of the surrounding mantle due to thermal equilibration (e.g., Irifune & Ringwood, 1993; Kirby et al., 1996; Ringwood, 1991). Consequently, the temperature effects are vital to constrain the slab dynamics. Nevertheless, our limited knowledge about the temperature dependence of the Al_2O_3 solubility in bridgmanite prevents us from understanding the mineralogy in the deep subducted slabs.

The reason for our limited knowledge about the temperature dependence of the Al_2O_3 solubility in bridgmanite is the technical difficulty in high-pressure and high-temperature experiments. Although use of the multi-anvil technique is desired for the determination of phase transitions in multiple-component systems, the pressure ranges of conventional multi-anvil presses are restricted to 27 GPa at high temperatures due to the limited hardness of tungsten carbide (WC) anvils. However, recent development of high-pressure and high-temperature technology using sintered-diamond (SD) anvils in conjunction with in situ synchrotron X-ray diffraction observations allows generation of accurate pressures up to 50 GPa routinely at high temperature (Liu et al., 2016; Tange et al., 2008). By utilizing these techniques, we have investigated phase relations in the system $\text{MgSiO}_3\text{-Al}_2\text{O}_3$ at temperatures up to 2300 K and pressures up to 45 GPa. Based on our new results, the Al_2O_3 solubility in bridgmanite and the host phases of Al_2O_3 in the lower mantle are discussed.

2. Experimental Methods

A fine-grained oxide mixture of composition $\text{En}_{50}\text{Cor}_{50}$ (En: MgSiO_3 , Cor: Al_2O_3 ; the number represents mol %, oxide grain size: 50 nm) and $\text{En}_{75}\text{Cor}_{25}$ glass (pyrope composition, hereafter denoted as pyropic glass) along the $\text{MgSiO}_3\text{-Al}_2\text{O}_3$ join are used as starting materials. Detailed chemical compositions of those two starting materials were reported in Liu et al. (2016) and also examined using an electron probe microanalyzer in the present study (see Table S1 in the supporting information). The starting materials were put into graphite or platinum capsules and then heated at 800 K for 1 h to purge water and finally put into the cell assembly for the high-pressure and high-temperature experiments.

In situ X-ray diffraction (XRD) experiments were performed at pressures of 32–49 GPa at temperatures of 1700 and 2000 K using SD anvils with 1.5 mm truncation as second-stage anvils in a DIA-type multi-anvil apparatus at the synchrotron radiation facility, SPring-8 (SPEED-Mk. II). The experimental facility for in situ XRD measurements was described by Katsura et al. (2004), and the ultrahigh pressure cell assembly was identical to that of Tange et al. (2009), as also shown in Figure 1. Pressures were determined based on the $P\text{-}V\text{-}T$ equation of state

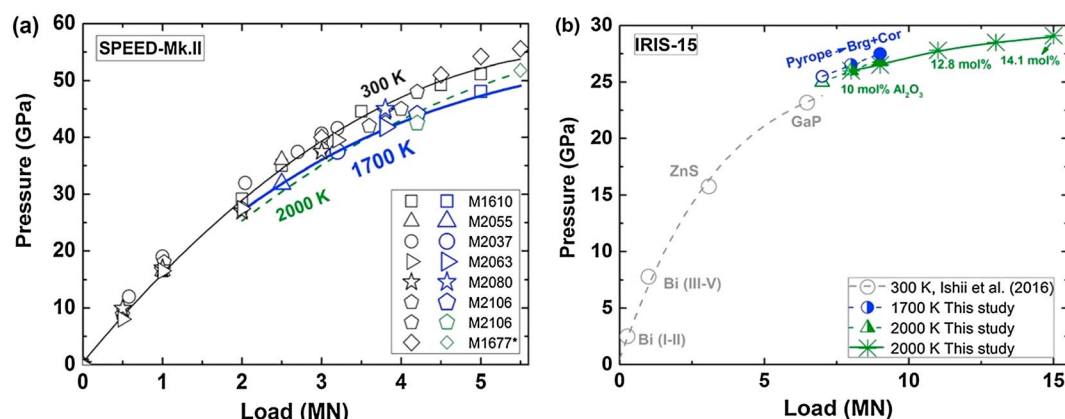


Figure 2. (a) Generated pressure versus the press load at room temperature (300 K, open black symbols), 1700 (blue symbols, this study), and 2000 K (green symbols, this study) for in situ XRD experiments using a DIA-type apparatus (SPEED-Mk.II) at SPring-8. The black and blue solid lines represent the fitting results of the data at 300 and 1700 K in the present study and that at 2000 K together with the symbol of M1677 is from Liu et al. (2016). (b) Pressure calibration curve at 1700 (circle) and 2000 K (triangle) for the IRIS-15 multianvil apparatus, based on the phase transition of pyrope to bridgmanite and corundum (Hirose et al., 2001) and various Al₂O₃ solubility (mol %) in bridgmanite at 2000 K (Liu et al., 2016). Pressure calibration at room temperature condition is from Ishii et al. (2016).

of Au proposed by Tsuchiya (2003). General relations between the generated pressure and the press load at temperatures of 300, 1700, and 2000 K are shown in Figure 2a. Uncertainties in pressure determination in these in situ experiments are approximately ± 0.2 GPa. Sample temperatures were measured with a W₉₇Re₃-W₇₅Re₂₅ thermocouple, whose hot junction was placed on the bottom of the sample capsule. The sample was compressed to the target pressure and then heated at the target temperature for 3–5 h. In situ XRD patterns were collected for 3–5 h at the target pressure and temperature. Then, the run was quenched by turning off the electronic power, and the pressure was released slowly over several hours. Finally, in situ XRD patterns of the quenched samples were collected under ambient conditions for 1 h.

We also conducted high-pressure quench experiments at the Bayerisches Geoinstitut, University of Bayreuth, Germany. Runs at pressures below 25 GPa were conducted using WC anvils with a 10.0 mm octahedral pressure medium and 4.0 mm anvil truncation in a 12-MN multianvil press with a split-sphere guide block (Sumitomo 1,200 t) (Keppler & Frost, 2005). One run conducted at a pressure of 35 GPa and a temperature of 2300 K was also performed using WC anvils with 1.5 mm truncation with this press. This pressure at 2300 K was estimated from the FeO content in bridgmanite (Tange et al., 2009), in equilibrium with magnesiowüstite and stishovite, using synthetic (Mg_{0.7}Fe_{0.3})SiO₃ pyroxene as a starting material (see Text S1 and Figure S1 in the supporting information for pressure calibration details). Runs at pressures above 25 GPa were performed using a 7 and 5.7 mm pressure medium and 3 and 1.5 mm truncation, respectively, in a 15-MN press with a DIA-type guide block system (IRIS-15) (Ishii et al., 2016). Figure 2b shows the relationships between pressures and press loads at temperatures of 1700 and 2000 K for IRIS-15, which were calibrated using decomposition of pyrope into aluminous bridgmanite and corundum (Hirose et al., 2001) and the Al₂O₃ solubility in bridgmanite (Liu et al., 2016). Pressure uncertainties of these quench experiments were on the order of ± 0.5 GPa.

Recovered samples were mounted in epoxy resin, ground to expose the central portion, and then polished using 0.25 μ m diamond paste. Phases present in the quench runs were identified using a microfocused X-ray diffractometer (XRD, Bruker, D8 DISCOVER) equipped with a two-dimensional solid-state detector (VANTEC500) and a microfocus source (μ S) with Co-K α radiation operated at 40 kV and 500 μ A. The X-ray beams were focused to 50 μ m using a Institute for Scientific Instruments (IFG) polycapillary X-ray minilens. Textural observation was performed using a LEO1530 scanning electron microscope operating at an acceleration voltage of 15–20 kV and a beam current of 10 nA. Chemical compositions of each phase present in the quench runs were determined using a JEOL JXA-8200 electron probe microanalyzer (EPMA) operating at acceleration voltages of 10 or 15 kV and a beam current of 5 nA with standards of enstatite for Mg and Si, and pyrope for Al.

Table 1
Experimental Run Conditions and Products

Run no.	Starting sample	Pressure (GPa)	Temperature (K)	Duration (h)	Phases
S6778	En ₅₀ Cor ₅₀ oxide	20	1700	6	Gar + Cor
S6607	En ₅₀ Cor ₅₀ oxide	25	1700	6	Gar + Cor
	En ₇₅ Cor ₂₅ glass				Gar
S6636	En ₅₀ Cor ₅₀ oxide	24	2300	3	Gar + Cor
IRIS232	En ₅₀ Cor ₅₀ oxide	27	1700	5	Al-Brg + Cor
IRIS266	En ₅₀ Cor ₅₀ oxide	27	1700	15	Al-Brg + Cor
	En ₇₅ Cor ₂₅ glass				Al-Brg + Cor + tr (Sti)
IRIS276	En ₅₀ Cor ₅₀ oxide	27	1900 ^a	2	Al-Brg + Cor
IRIS256	En ₅₀ Cor ₅₀ oxide	27	2000	5	Al-Brg + Cor
	En ₇₅ Cor ₂₅ glass				Al-Brg + Cor
IRIS244	En ₅₀ Cor ₅₀ oxide	27	2300	2	Al-Brg + Cor + tr (Sti)
	En ₇₅ Cor ₂₅ glass				Al-Brg + Cor
IRIS300	En ₅₀ Cor ₅₀ oxide	27	2500 ^a	0.5	Al-Brg + Cor + tr (Sti)
	En ₇₅ Cor ₂₅ glass				Al-Brg + Cor
IRIS252	En ₅₀ Cor ₅₀ oxide	30	2300	1.5	Al-Brg + Cor
M2055	En ₅₀ Cor ₅₀ oxide	31.9	1700	5	Al-Brg + Cor
S6615	En ₅₀ Cor ₅₀ oxide	35	2300	1.5	Al-Pv + Cor
M2037	En ₅₀ Cor ₅₀ oxide	38.5	1700	5.5	Al-Brg + Cor
M2063	En ₅₀ Cor ₅₀ oxide	41.8	1700	6	Al-Brg + Cor
M2080	En ₇₅ Cor ₂₅ glass	44.8	1700	5	Al-Brg + Cor + tr (Sti)
M2106	En ₇₅ Cor ₂₅ glass	42.3	2000	3	Al-Brg + Cor + tr (Sti)
M1610	En ₅₀ Cor ₅₀ oxide	48.5	1700 ^b	2	Al-Brg + Cor + tr (Sti)
M1677 ^c	En ₅₀ Cor ₅₀ oxide	51.8	2000	3	Al-Brg + Cor

Note. Abbreviations: Gar: garnet, Cor: corundum, Sti: stishovite, Al-Brg: aluminous bridgmanite, Al-Pv: aluminous perovskite; and tr: trace.

^aTemperature was evaluated from a calibrated power curve derived from the low temperature of 1500 K for IRIS276 and 2400 K for IRIS300. ^bTemperature is around 1700–1800 K due to the instability of the heater. ^cThe run is from Liu et al. (2016).

3. Results

Experimental conditions and phases present in the recovered samples are listed in Table 1. At pressures below 25 GPa under temperatures of 1700 and 2300 K, the starting material of En₅₀Cor₅₀ transforms into pyrope and corundum (see Figure S2 in the supporting information), and these corundum can contain significant amounts of the MgSiO₃ component (see Table S2 in the supporting information). The MgSiO₃ solubility in corundum increases with increasing pressure and temperature, for example, 7.9 ± 0.4 mol % at 20 GPa to 12.6 ± 0.6 mol % at 25 GPa under a temperature of 1700 K and 12.6 ± 0.6 mol % at 1700 K to 26.7 ± 0.7 mol % at 2300 K under a pressure of 25 GPa.

Figure 3a shows representative backscattered electron images of the quenched samples for En₅₀Cor₅₀ oxide mixture and pyropic glass at a pressure of 27 GPa and at temperatures of 1700 and 2500 K, respectively. The corresponding XRD profiles in Figures 3b and S2 (see supporting information) of these run products are consistent with the presence of a mixture of bridgmanite and corundum. As shown in Table 2, the chemical compositions of phases in the recovered samples using these two different starting materials are identical within analytical uncertainties, implying that chemical equilibrium was achieved under these conditions.

Figure 4 illustrates the solubility of Al₂O₃ in bridgmanite and that of MgSiO₃ in corundum, respectively, as a function of temperatures at a constant pressure of 27 GPa as determined in the present and previous studies (Akaogi et al., 2002; Irifune et al., 1996; Kubo & Akaogi, 2000; Liu et al., 2016). The Al₂O₃ solubility in bridgmanite apparently increases linearly with temperature (Figure 4a), and this tendency is similar to that for FeO in bridgmanite reported by Fei et al. (1996). In the present study, the Al₂O₃ solubility in bridgmanite reaches 21.7 ± 0.6 mol % at 2500 K. The best fit of all the experimental data to a linear function yields the relation of $X_{\text{Al}_2\text{O}_3} = -0.19(2) + 1.60(1) \cdot 10^{-5} \cdot T$, where $X_{\text{Al}_2\text{O}_3}$ is the Al₂O₃ solubility in mole percent in bridgmanite at a pressure of 27 GPa, T is the temperature in kelvin, and the number in parentheses represents standard deviations for the last digit. This equation suggests that bridgmanite with a pyrope composition, that is, with 25 mol % Al₂O₃, could form at a temperature of approximately 2750 K at this pressure. Figure 4b

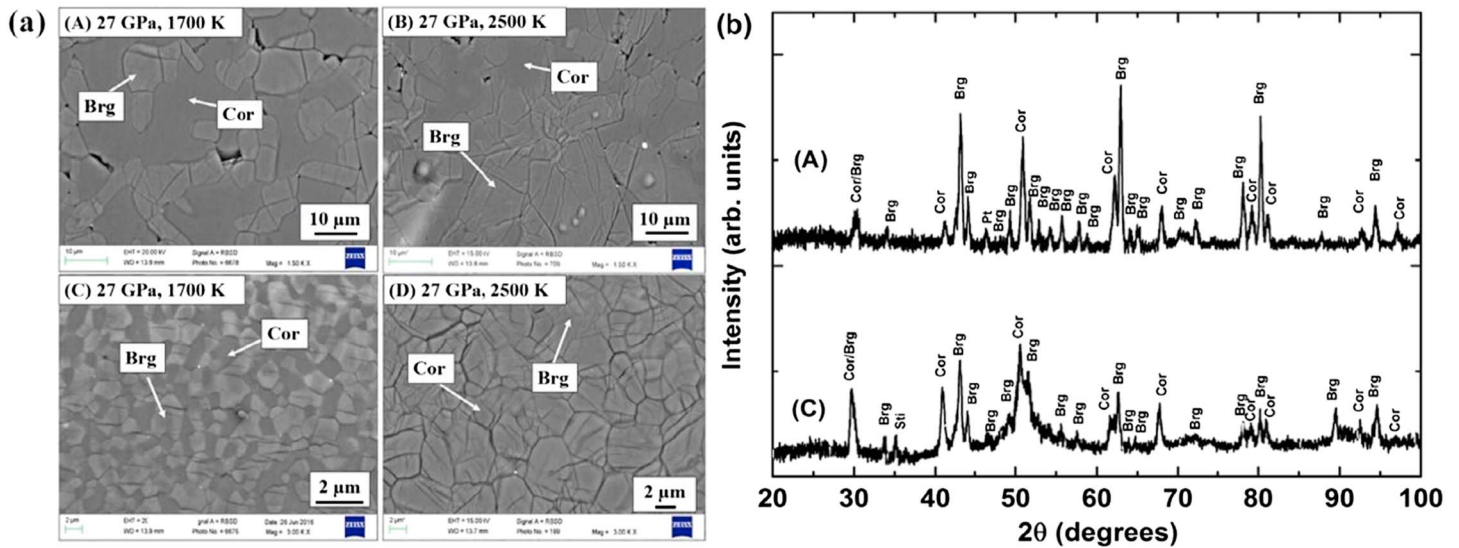


Figure 3. (a) Representative backscattered electron images of the run products for En₅₀Cor₅₀ (A and B) and pyropic compositions (C and D) synthesized at 27 GPa and 1700 and 2500 K, respectively. (b) Selected XRD patterns of the run products of (A) En₅₀Cor₅₀ and (C) pyropic compositions at 27 GPa and 1700 K, respectively. Abbreviations: Brg, bridgmanite; Cor, corundum; and Sti, stishovite.

Table 2

Chemical Compositions of the Coexisting Mineral Phases in the Run Products at Pressure Above 27 GPa

Run no.	Start comp	Phases	MgO	Al ₂ O ₃	SiO ₂	Total	Mg	Al	Si	Sum
IRIS232	En ₅₀ Cor ₅₀	Brg (<i>n</i> = 15)	37.79 (62)	6.79 (41)	55.33 (78)	99.11 (115)	3.776 (35)	0.521 (35)	3.722 (19)	8.018 (13)
		Cor (<i>n</i> = 12)	6.73 (33)	82.46 (90)	9.19 (69)	98.18 (45)	0.671 (35)	6.706 (48)	0.635 (37)	8.012 (19)
IRIS266	En ₅₀ Cor ₅₀	Brg (<i>n</i> = 15)	37.45 (66)	6.93 (36)	55.33 (88)	99.80 (132)	3.754 (26)	0.548 (32)	3.714 (17)	8.014 (19)
		Cor (<i>n</i> = 12)	6.84 (49)	82.07 (27)	9.91 (42)	98.82 (70)	0.699 (56)	6.629 (60)	0.679 (26)	8.006 (17)
IRIS256	En ₅₀ Cor ₅₀	Brg (<i>n</i> = 11)	35.67 (26)	12.49 (27)	52.94 (25)	101.10 (63)	3.523 (48)	0.975 (25)	3.507 (14)	8.005 (19)
		Cor (<i>n</i> = 12)	9.74 (29)	74.98 (17)	14.58 (42)	99.05 (57)	0.989 (28)	6.017 (37)	0.993 (24)	7.999 (12)
IRIS276	En ₅₀ Cor ₅₀	Brg (<i>n</i> = 10)	35.36 (27)	11.66 (14)	52.40 (45)	99.42 (81)	3.552 (10)	0.925 (6)	3.530 (7)	8.007 (5)
		Cor (<i>n</i> = 10)	8.61 (37)	79.26 (28)	12.67 (23)	100.54 (46)	0.864 (34)	6.287 (13)	0.853 (17)	8.004 (17)
IRIS244	En ₅₀ Cor ₅₀	Brg (<i>n</i> = 15)	31.50 (54)	20.60 (24)	49.97 (56)	98.79 (93)	3.243 (33)	1.541 (28)	3.222 (14)	8.007 (12)
		Cor (<i>n</i> = 12)	13.08 (17)	67.41 (29)	18.30 (31)	98.80 (19)	1.335 (15)	5.439 (34)	1.253 (19)	8.027 (4)
	En ₇₅ Cor ₂₅	Brg (<i>n</i> = 15)	33.34 (38)	20.04 (35)	49.37 (27)	102.75 (39)	3.243 (33)	1.541 (28)	3.222 (14)	8.007 (12)
		Cor (<i>n</i> = 12)	11.74 (17)	68.73 (39)	17.51 (31)	98.27 (73)	1.203 (12)	5.586 (34)	1.204 (37)	8.000 (14)
IRIS300	En ₅₀ Cor ₅₀	Brg (<i>n</i> = 15)	31.39 (36)	22.38 (52)	47.46 (51)	101.24 (59)	3.100 (31)	1.735 (49)	3.149 (28)	7.984 (11)
		Cor (<i>n</i> = 12)	15.08 (11)	63.14 (83)	23.09 (28)	101.33 (79)	1.497 (7)	4.953 (33)	1.537 (24)	7.987 (8)
	En ₇₅ Cor ₂₅	Brg (<i>n</i> = 15)	31.25 (49)	22.09 (25)	46.97 (31)	100.28 (76)	3.114 (32)	1.740 (18)	3.138 (16)	7.992 (15)
		Cor (<i>n</i> = 12)	14.69 (42)	63.72 (63)	22.10 (128)	100.21 (121)	1.474 (26)	5.034 (93)	1.487 (68)	7.996 (18)
IRIS252	En ₅₀ Cor ₅₀	Brg (<i>n</i> = 15)	32.32 (55)	21.66 (69)	47.58 (79)	101.56 (125)	3.183 (31)	1.687 (53)	3.143 (31)	8.013 (11)
		Cor (<i>n</i> = 12)	10.97 (30)	72.26 (74)	15.93 (44)	99.16 (26)	1.115 (32)	5.808 (73)	1.086 (31)	8.009 (11)
S6615	En ₅₀ Cor ₅₀	Brg (<i>n</i> = 8)	29.69 (49)	27.76 (23)	42.55 (32)	100 ^a	2.983 (22)	2.197 (17)	2.861 (38)	8.041 (14)
		Cor (<i>n</i> = 10)	8.82 (19)	77.76 (34)	12.44 (25)	99.01 (37)	0.899 (12)	6.277 (25)	0.854 (15)	8.016 (5)
M2055	En ₅₀ Cor ₅₀	Brg (<i>n</i> = 8)	35.26 (27)	11.76 (24)	52.71 (39)	99.73 (58)	3.530 (29)	0.930 (17)	3.538 (21)	7.997 (13)
		Cor (<i>n</i> = 10)	4.75 (51)	87.84 (45)	6.83 (48)	99.42 (81)	0.482 (29)	7.058 (57)	0.465 (29)	8.006 (3)
M2037	En ₅₀ Cor ₅₀	Brg (<i>n</i> = 8)	34.52 (27)	13.72 (40)	51.82 (56)	99.96 (53)	3.414 (17)	1.195 (23)	3.397 (19)	8.005 (12)
		Cor (<i>n</i> = 10)	4.50 (49)	90.10 (53)	6.72 (51)	101.12 (76)	0.450 (36)	7.118 (48)	0.437 (32)	8.004 (5)
M2063	En ₅₀ Cor ₅₀	Brg (<i>n</i> = 5)	34.27 (77)	15.41 (54)	50.95 (90)	101.64 (89)	3.369 (54)	1.275 (22)	3.359 (22)	8.003 (24)
		Cor (<i>n</i> = 11)	3.61 (28)	92.41 (62)	5.23 (22)	101.37 (51)	0.360 (22)	7.283 (34)	0.358 (15)	8.001 (2)
M2106	En ₇₅ Cor ₂₅	Brg (<i>n</i> = 8)	31.55 (69)	22.35 (82)	46.99 (82)	100.89 (98)	3.127 (57)	1.751 (38)	3.124 (47)	8.001 (33)
M1677	En ₅₀ Cor ₅₀	Brg (<i>n</i> = 12)	28.08 (47)	30.00 (64)	42.57 (69)	100.63 (30)	2.789 (58)	2.357 (48)	2.838 (38)	7.984 (27)
		Cor (<i>n</i> = 16)	4.62 (58)	88.98 (80)	6.40 (52)	100.01 (17)	0.467 (6)	7.110 (60)	0.434 (35)	8.010 (23)

Note. Oxide analyses are reported in wt %. Cations are reported based on the oxygen number is normalized to 12. Number in parentheses represents standard deviation and is placed in the last digit(s). *n*: the number of analysis points. Abbreviations: Brg, bridgmanite; Cor, corundum; and Comp, composition.

^aNormalized to 100 due to some amounts (~1 wt %) of WO₃ in bridgmanite.

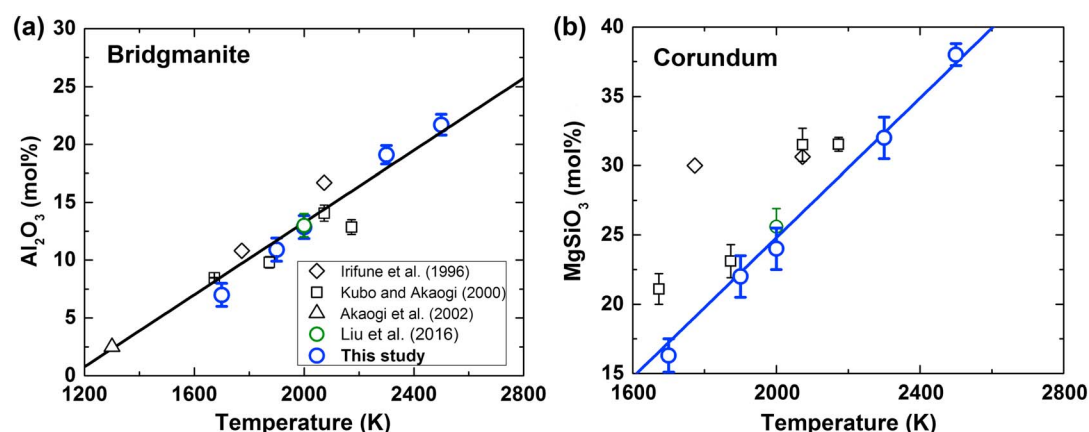


Figure 4. (a) Al_2O_3 solubility in bridgmanite and (b) MgSiO_3 solubility in corundum, respectively, as a function of temperature at a constant pressure of 27 GPa. The solid black and blue lines are the least squares fitting of all the data and only the data in the present study, respectively.

demonstrates that the MgSiO_3 solubility in corundum also increases with increasing temperature at 27 GPa and reaches as much as 38.0 ± 0.5 mol % at 2500 K in the present study. The values for corundum reported by Irifune *et al.* (1996) and Kubo and Akaogi (2000) are, however, larger than those in the present study at given the same temperature. One possible reason for this discrepancy may be related to the low resolution of the EPMA due to the small grain sizes of corundum and bridgmanite obtained in earlier studies. The grain size of phases in the runs at 27 GPa in our study is considerably larger than $3 \mu\text{m}$ in Figure 3; the composition is thus accurate due to the grain size is larger than the resolution of the EPMA.

Figure 5 shows selected backscattered electron images of the quenched samples for the $\text{En}_{50}\text{Cor}_{50}$ oxide mixture and pyropic glass at pressures higher than 27 GPa. Aluminous bridgmanite, corundum, and Au pressure markers are found in these in situ runs. Figure 6a shows in situ synchrotron XRD patterns for $\text{En}_{50}\text{Cor}_{50}$ under 31.9–48.5 GPa at 1700 K. In all XRD patterns, the major peaks are assigned to bridgmanite, corundum, and Au, while the other minor ones can be assigned to stishovite, surrounding diamond capsules, and MgO disks. For the product recovered from the run at 48.5 GPa and 1700 K for 2 h, the element mapping by means of analytical transmission electron microscopy reported in Figure S3 further confirms that bridgmanite, corundum and trace amount of stishovite coexist in this sample. However, the transmission electron microscopy (TEM) mapping combined with energy dispersive X-ray spectroscopy suggest that the compositions of these phases are not homogeneous, which may be caused by the unreached chemical equilibrium due to the short heating time as a result of the instability of the heater in this run (Text S2). Figure 6b shows the XRD pattern of the S6615 run. It is found that perovskite with a LiNbO_3 structure with a rhombohedral symmetry coexists with corundum at 35 GPa and 2300 K. EPMA analysis on this LiNbO_3 structure demonstrates that it contains 27.3 ± 0.3 mol % of Al_2O_3 . Its lattice parameters ($a = b = 4.849$ (1); $c = 12.712$ (10)) are slightly higher than those ($a = b = 4.783$ (2); $c = 12.680$ (11)) for the same phase with the pyrope composition obtained by Liu *et al.* (2016), which can be explained by a higher Al_2O_3 content in the present study than that of the latter study. The present result further confirms that bridgmanite with the Al_2O_3 content higher than 25 mol % would transform into the LiNbO_3 structure upon releasing pressure, which is consistent with the result of earlier works (Funamori *et al.*, 1997; Ishii *et al.*, 2017; Liu *et al.*, 2016; Miyajima *et al.*, 1999). However, Liu *et al.* (2016) also found that the bridgmanite phase containing 29.5 mol % exists in the M1677 run, and this difference may be caused by the effect of nanoscale grain size with a higher surface energy as suggested by Liu *et al.* (2016).

Two experiments were performed using the pyropic glass as the starting material at pressures of 42.3 and 44.5 GPa and at temperatures of 2000 and 1700 K, respectively (Figure 6c). In situ XRD observations suggest that the phases present in these runs are bridgmanite and corundum. In particular, a trace amount of corundum coexists with bridgmanite at 42.3 GPa and 2000 K, which is also confirmed by the backscattered electron observations in Figure 5d. Composition analysis on several large grains ($3 \mu\text{m}$) suggests that bridgmanite in this recovered sample contains 21.9 ± 0.6 mol % Al_2O_3 . These results suggest that bridgmanite with the pyrope composition should form at a slightly higher pressure than 42.3 GPa, providing more convincing

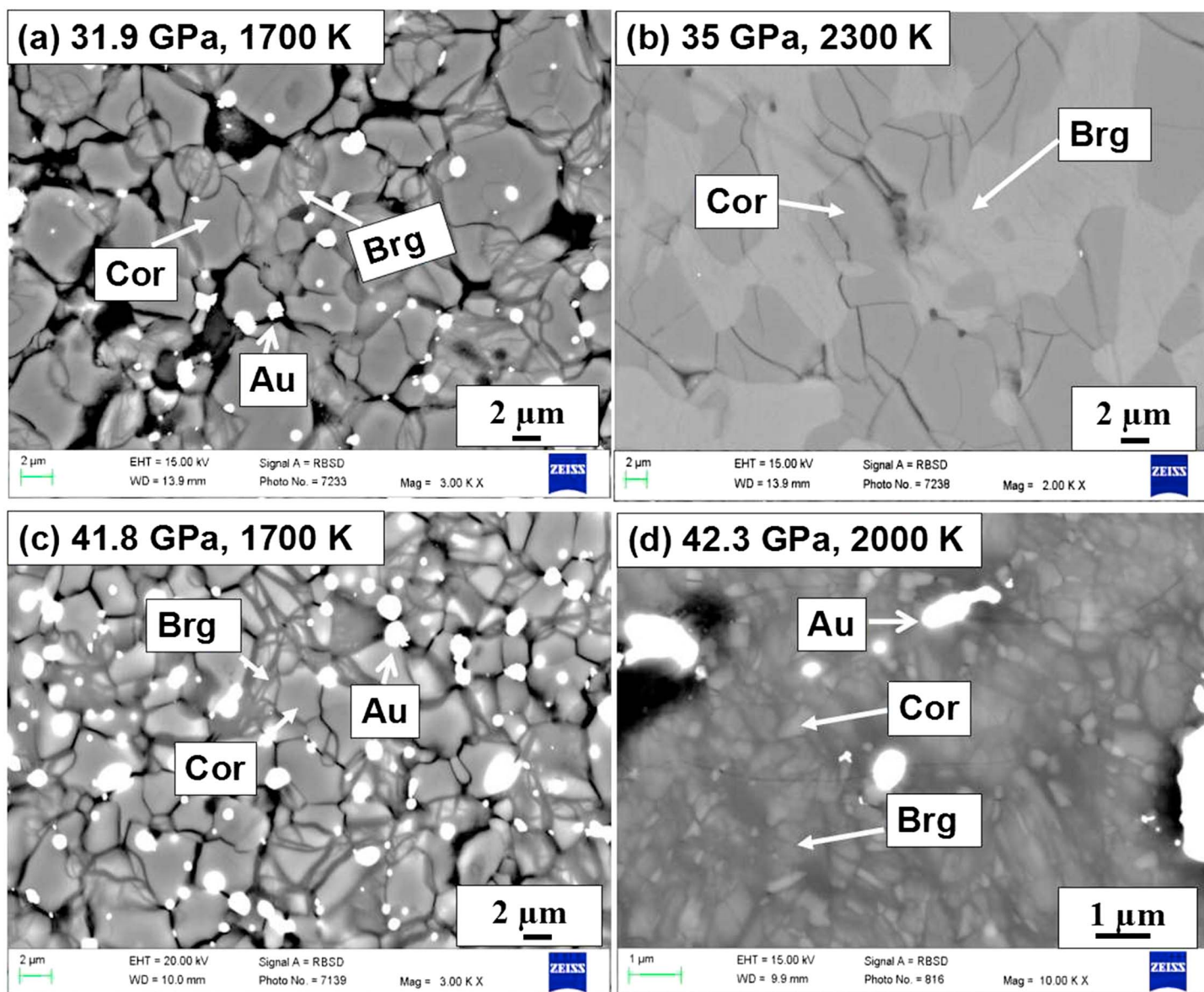
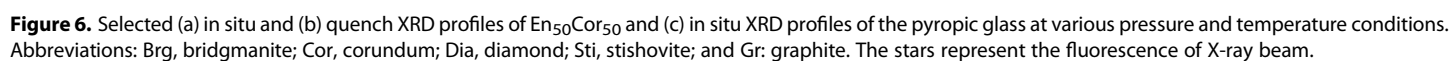


Figure 5. Selected backscattered electron images of the run products for (a–c) $\text{En}_{50}\text{Cor}_{50}$ at 31.9–41.8 GPa and 1700 and 2300 K and (d) pyropic glass at 42.3 GPa and 2000 K. Abbreviations: Brg, bridgmanite; Cor, corundum; and Au: gold.

evidence that the Al_2O_3 solubility exceeds 25 mol % above 45 GPa at 2000 K (Liu et al., 2016). The composition of bridgmanite in M1677 run (51.8 GPa and 2000 K) in Liu et al. (2016) was estimated based on relations between unit lattice parameters and Al_2O_3 contents. Here instead, we determined the accurate compositions of the phases in M1677 run by adjusting the EPMA analytical beam size to 1 μm and found that the Al_2O_3 content in bridgmanite is 29.5 ± 0.7 mol %, in excellent agreement with that (29 ± 5 mol %) estimated from its unit cell lattice parameters. Therefore, for the sample at 44.5 GPa and 1700 K, since the grain size of this run product is smaller than 1 μm , the Al_2O_3 content in bridgmanite has been estimated to be approximately 16 ± 3 mol % from its unit cell lattice parameters (see Table S3 in the supporting information) (Liu et al., 2016).

The lattice parameters and molar volume of aluminous bridgmanite and corundum in the present and previous studies (D'Amour et al., 1978; Irifune et al., 1996; Ito et al., 1998; Ito & Matsui, 1978; Liu et al., 2016; Kubo & Akaogi, 2000; Walter et al., 2004; Weng et al., 1981; Yagi et al., 2004) are shown as a function of the Al_2O_3 and MgSiO_3 content, respectively, in Figure 7. It is clearly seen that the value of a , b , and c axis of



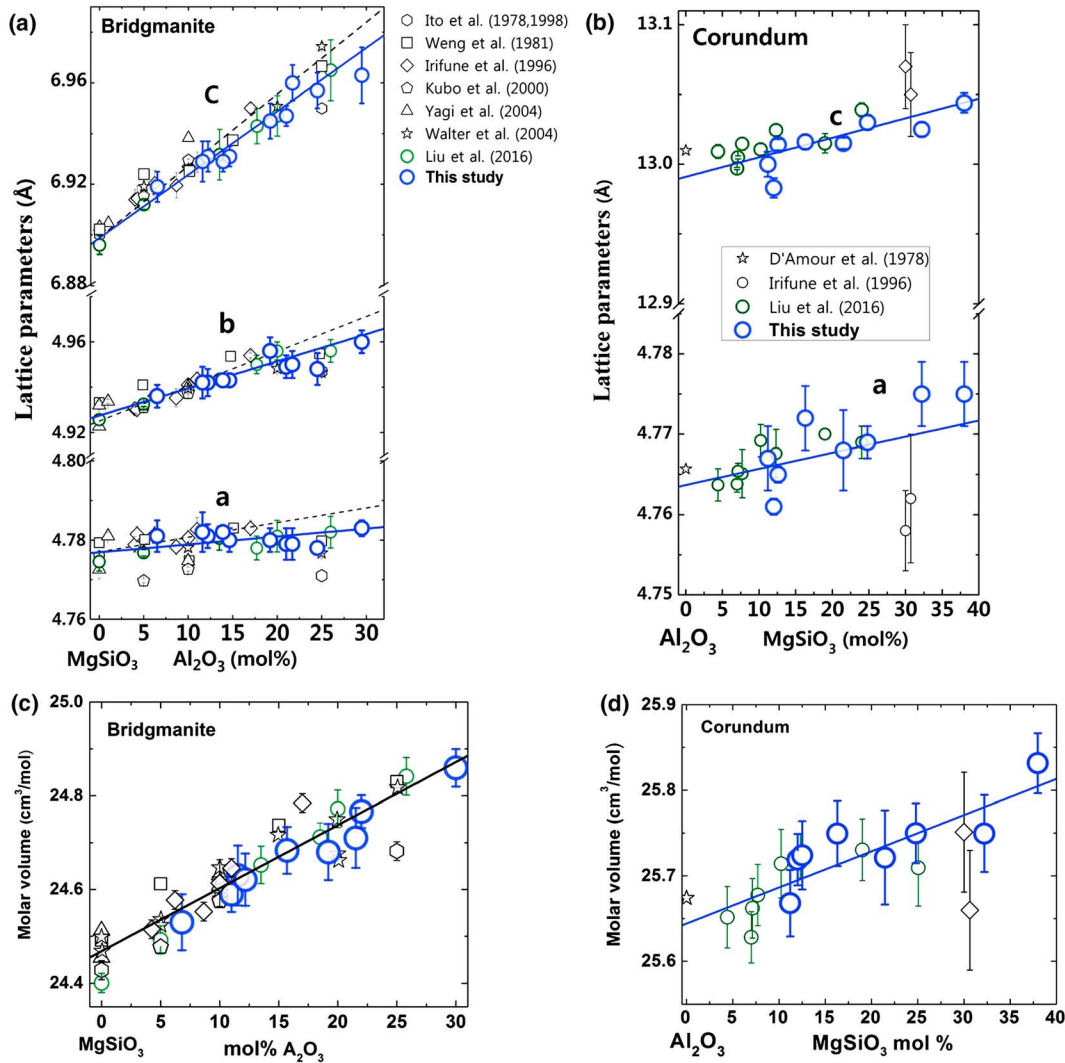


Figure 7. Lattice parameter and molar volume of (a and c) bridgmanite and (b and d) corundum versus the Al_2O_3 and MgSiO_3 content, respectively, in the present and previous work. Solid lines are the linear fitting of the present data and Liu et al. (2016), and the dashed lines are results of Irifune et al. (1996).

aluminous bridgmanite increases almost linearly with increasing Al_2O_3 content within analytical uncertainties in Figure 7a. A linear function is adapted to the present data and those of Liu et al. (2016) and got the following equations:

$$a = 4.777 (\pm 0.001) + 0.014 (\pm 0.007) \times \chi_{\text{Al}_2\text{O}_3}$$

$$b = 4.928 (\pm 0.002) + 0.109 (\pm 0.011) \times \chi_{\text{Al}_2\text{O}_3}$$

$$c = 6.900 (\pm 0.002) + 0.236 (\pm 0.012) \times \chi_{\text{Al}_2\text{O}_3},$$

where $\chi_{\text{Al}_2\text{O}_3}$ represents the mole fraction of the Al_2O_3 in bridgmanite ($0 \leq \chi_{\text{Al}_2\text{O}_3} < 0.30$). These equations agree well with those obtained in Irifune et al. (1996) except that the slope for the change in lattice parameters with the Al_2O_3 content is slightly smaller than that obtained in the latter study. The same equation to corundum produces following results (Figure 7b):

$$a = b = 4.764 (2) + 0.023(9) \times \chi_{\text{MgSiO}_3}$$

$$c = 12.991 (6) + 0.136 (3) \times \chi_{\text{MgSiO}_3},$$

where χ_{MgSiO_3} represents the mole fraction of the MgSiO_3 in bridgmanite ($0 \leq \chi_{\text{MgSiO}_3} < 0.4$). The molar volume of bridgmanite increases almost linearly with increasing Al_2O_3 contents (Figure 7c) and can be best expressed as $V(x) = 1.35 (8) \cdot x + 24.468 (12)$, where x is the mole fraction of Al_2O_3 ($0 \leq x < 0.3$), and the number

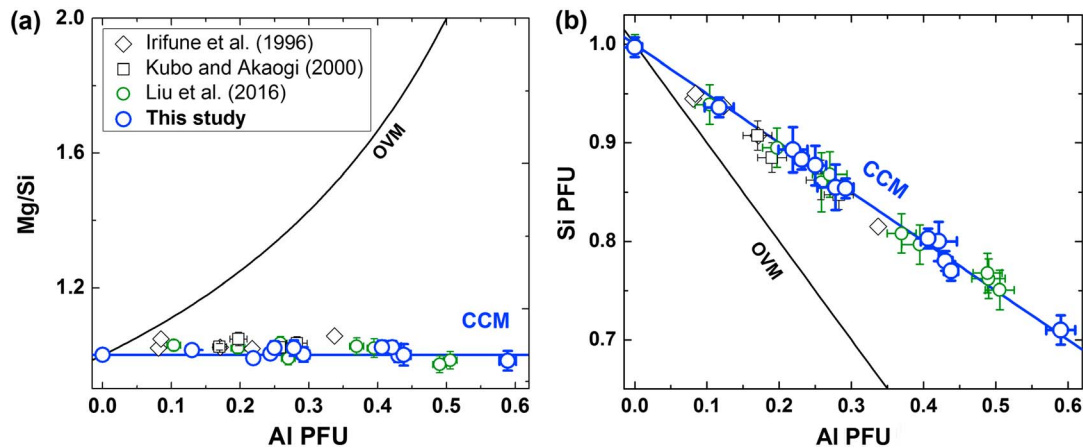


Figure 8. The ratio between (a) Mg and Si cation and (b) Si cation number versus the Al per formula unit (pfu, based on three oxygens) in bridgmanite in the present study and previous works (Irifune et al., 1996; Kubo & Akaogi, 2000; Liu et al., 2016). Solid blue and black lines indicate the trend expected for trivalent cation incorporation by the charge-coupled substitution mechanism and oxygen vacancy substitution mechanism, respectively.

in parentheses represents standard deviations for the last digit. It can be also seen in Figure 7d that the molar volume of corundum increases slightly with increasing MgSiO_3 contents, expressed as $V(x) = 0.42(7) \cdot x + 25.64(1)$, where x is the mole fraction of MgSiO_3 ($0 \leq x < 0.4$). The effect of MgSiO_3 contents on the volume of corundum is significantly smaller than that of Al_2O_3 for bridgmanite.

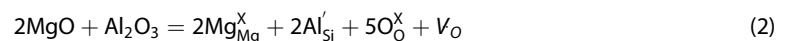
4. Discussion

4.1. Al Substitution Mechanism in Bridgmanite

It is thought that Al is incorporated into the crystal structure of bridgmanite through two types of possible substitution mechanisms (Andrault et al., 2007; Hirsch & Shankland, 1991; Navrotsky, 1999; Navrotsky et al., 2003; Richmond & Brodholt, 1998): (1) the charge-coupled substitution: substituting of Mg and Si by Al,



and (2) the oxygen vacancy substitution: substitution of Al into the Si site and creating an oxygen vacancy,



where subscripts indicate the site and superscripts indicate the charge (\times) for neutral, ($'$) for negative charge, (\cdot) for a positive charge (point defect notation from Kröger & Vink, 1956). Figure 8a shows the cation ratio between Mg and Si (Mg/Si) as a function of the Al per formula unit (pfu) in aluminous bridgmanite in the present study and previous works (Irifune et al., 1996; Kubo & Akaogi, 2000; Liu et al., 2016). This ratio is mainly along the trend line for the charge-coupled substitution within the analytical uncertainties, while it is far below the trend line of the oxygen vacancy substitution, suggesting the charge-coupled substitution dominates in the aluminous bridgmanite. This result is well consistent with some earlier experimental works on aluminous bridgmanite (Stebbins et al., 2001; Walter et al., 2006). Figure 8b further supports this idea due to the value of Si cation in the bridgmanite is almost along the trend line for the charge-coupled substitution. However, XRD patterns in such as Figures 3 and 6 demonstrate that trace stishovite coexisted with bridgmanite in some runs, suggesting that trace amounts of the oxygen vacancy substitution may also occurs in the aluminous bridgmanite.

4.2. Phase Diagram in the MgSiO_3 - Al_2O_3 System

Figure 9 shows the phase diagram of the garnet-corundum-bridgmanite transition in the system MgSiO_3 - Al_2O_3 at pressures of 20–45 GPa and at temperatures of 1700, 2000, and 2300 K. The pressure of the disproportionation of pyrope at various temperatures is estimated from the runs at 1700 and 2000 K in Figure 2b together with the study by Hirose et al. (2001). At pressures lower than 25 GPa at these three temperatures, $\text{En}_{50}\text{Cor}_{50}$ crystallizes an assemblage of pyrope plus corundum. Depending on temperatures, pyrope would decompose into bridgmanite and corundum at 25.5–27 GPa. At a pressure of 27 GPa at these

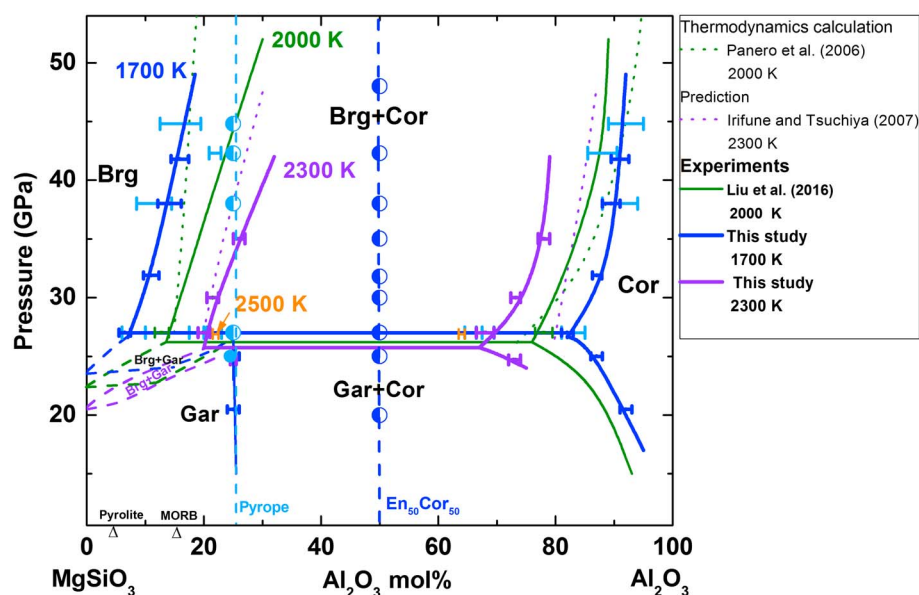


Figure 9. Phase relations in the MgSiO_3 - Al_2O_3 system at 24–45 GPa and 1700, 2000, and 2300 K in the present and previous studies. Dark and light blue dashed lines represent the chemical compositions of the starting materials in the present study. Dark blue circular symbols indicate the high-pressure runs using the $\text{En}_{50}\text{Cor}_{50}$ oxide mixture as the starting material, while light blue circular symbols indicate those for the pyropic glass. The corresponding horizontal lined symbols mark the compositions of the coexisting phases for the $\text{En}_{50}\text{Cor}_{50}$ oxide mixture and the pyropic glass. The phase loop of bridgmanite plus garnet was referenced from Irifune et al. (1996), Kubo and Akaogi (2000), and Irifune and Tsuchiya (2007). The triangles represent the Al_2O_3 content in the pyrolite and MORB models. Error bars indicate the uncertainties of chemical compositions. Abbreviations: Brg, bridgmanite; Cor, corundum; Sti, stishovite; and Gar, garnet.

temperatures, the two-phase field of bridgmanite and corundum is thus stabilized. At this pressure, the Al_2O_3 solubility in bridgmanite increases from 6.7 ± 0.5 to 21.7 ± 0.6 mol % with increasing temperature from 1700 to 2500 K. In the same temperature range, the MgSiO_3 solubility in corundum also increases from 16.3 ± 0.8 to 38.0 ± 0.5 mol %. Therefore, the two-phase region of bridgmanite and corundum becomes narrower with increasing temperature. The shrinkage of the two-phase region also occurs at higher pressures with increasing temperature. These shrinkages are related to the mixing entropy and enthalpy (Panero et al., 2006).

At a constant temperature, bridgmanite becomes more aluminous with increasing pressure. The Al_2O_3 solubility in bridgmanite increases from 6.7 ± 0.5 to 16 ± 3 mol % with increasing pressure from 27 to 44.5 GPa at 1700 K, from 12.2 ± 0.3 to 21.9 ± 0.6 mol % for pressures from 27 to 42.3 GPa at 2000 K and from 19.2 ± 0.4 to 27.3 ± 0.3 mol % for pressures from 27 to 35 GPa at 2300 K. In contrast, the MgSiO_3 content in corundum decreases with increasing pressure, for example, 16.4 ± 0.8 to 7 ± 4.0 mol % at 1700 K and 32.2 ± 0.4 to 21.7 ± 0.5 mol % at 2300 K. Both Al_2O_3 and MgSiO_3 enrichment in bridgmanite and corundum, respectively, can be explained by the cation substitution in the crystal structure of bridgmanite and corundum (e.g., Brodholt, 2000; Kubo & Akaogi, 2000; Liu et al., 2016; Walter et al., 2004).

Increasing proportions of the Al_2O_3 and MgSiO_3 components in bridgmanite and corundum, respectively, increases the lattice parameters of each of the phases (Figures 7a and 7b). The lower molar volume of bridgmanite (about 64% of the corundum volume) results in the partitioning of alumina into bridgmanite coexisting with increasingly alumina-rich corundum as pressure increases, accompanied by an increased ratio of bridgmanite to corundum. A simple lever rule analysis of the phase diagram in Figure 9 rationalizes the variations in phase compositions and proportions as a function of pressure. The opposite situation is seen for the coexisting garnet-corundum assemblage. With bulk system compositions within the two-phase field, the garnet is fixed at the pyrope composition (25 mol % Al_2O_3), and the proportion of garnet decreases with increasing pressure as the MgSiO_3 content of the coexisting corundum increases.

The phase boundaries between bridgmanite and two-phase region of bridgmanite and corundum at 2000 and 2300 K, respectively, reported in the present study are close to those obtained using thermodynamics calculation by Panero et al. (2006) and prediction by Irifune and Tsuchiya (2007), respectively, although the

rate of the increasing Al_2O_3 content in bridgmanite with increasing pressure in the present study is slightly larger than that in the calculation and prediction. On the contrary, the phase boundary between this two-phase region and corundum is largely different from that obtained in the mentioned calculation and prediction, which may be caused by the poorly constrained thermodynamics parameters of corundum.

We note that the compositions of the phases in the recovered samples from experiment runs with the pyro-pic glass as the starting material are identical to those recovered from experiments for the $\text{En}_{50}\text{Cor}_{50}$ oxide mixture within analytical errors, as shown in Figure 9. This fact suggests that chemical equilibrium was achieved in our study. This idea is also supported by the identical compositions of two phases obtained from a shorter (5 h, IRIS232) and longer (15 h, IRIS266) heating duration at the same conditions.

4.3. Host Phases of Al_2O_3 in the Lower Mantle

Here we discuss the Al_2O_3 host phases in the lower mantle at depths between 750 and 1,250 km, corresponding to pressures of 27 and 50 GPa, respectively. The representative lower mantle temperatures at these depths are approximately 2000 K (Katsura et al., 2010). Temperatures in subducted slabs under lower mantle pressures are unknown but must be substantially lower than these ambient-mantle temperatures (Kirby et al., 1996).

The pyrolite composition contains about 4 wt % of Al_2O_3 (Sun, 1982). The phase diagram in Figure 9 suggests that bridgmanite can contain 13 and 29 wt % of Al_2O_3 at a depth of 750 and 1,250 km, respectively. Therefore, all Al_2O_3 should be accommodated in bridgmanite in the majority of the lower mantle, as already suggested by Irifune (1994). In subducted slabs, the estimated temperature profile may be at least 300 K lower than the ambient mantle depending on whether the slabs are young or old (Kirby et al., 1996). At these lower temperatures, the Al_2O_3 solubility in bridgmanite is about 7 and 17 wt %, at depth of 750 and 1,250 km, respectively. Moreover, the MORB parts of slabs have an Al_2O_3 content up to 16 wt % (Green et al., 1979). Therefore, all Al_2O_3 cannot be fully accommodated in the cold peridotite parts of subducted slabs at 750 km depth, and one additional aluminous phase such as the CF (a MgAl_2O_4 dominated phase with a calcium ferrite-type structure) (Irifune et al., 1991) may therefore form to host the excess Al_2O_3 in this region. At a depth of 1250 km, however, the Al_2O_3 solubility exceeds 16 wt % even at lower temperature, and therefore, CF is expected to disappear with increasing subduction depth.

Although phase relations in the MgSiO_3 - Al_2O_3 system have been determined as a function of pressure and temperature by our advanced multianvil experiments using SD technology and in situ synchrotron XRD, the chemical systems in the lower mantle and subducted slabs are more complicated. The FeSiO_3 and FeAlO_3 components may change the Al_2O_3 solubility in bridgmanite (e.g., Kesson et al., 1995; Miyajima et al., 1999; Nishio-Hamane et al., 2005). In particular, the dominance of the FeAlO_3 component in bridgmanite should change the Al_2O_3 solubility relative to that in the MgSiO_3 - Al_2O_3 system (Miyajima et al., 1999; Nishio-Hamane et al., 2005). The presence of K_2O and Na_2O components would stabilize CF and NAL phases as host phases for the Al_2O_3 component in MORB slabs (e.g., Hirose & Fei, 2002; Irifune & Ringwood, 1993; Litasov & Ohtani, 2005; Miyajima et al., 1999, 2001; Ono et al., 2001), which would decrease the Al_2O_3 contents in bridgmanite. Therefore, further studies of phase relations in Fe-, K-, and Na-bearing systems are needed to constrain the host phases of Al_2O_3 and their compositions in the lower mantle.

5. Conclusion

Phase relations in the system MgSiO_3 - Al_2O_3 were determined at pressures between 27 and 45 GPa and temperatures of 1700, 2000, and 2300 K. At pressure just below 27 GPa, phase assemblages of garnet + bridgmanite and garnet + corundum are stable for compositions of less and more than 25 mol % Al_2O_3 . At pressures above 27 GPa, another assemblage of bridgmanite and corundum is stabilized for bulk compositions within the two-phase field. The Al_2O_3 and MgSiO_3 solubility in bridgmanite and corundum, respectively, increases with increasing temperature. Moreover, bridgmanite becomes more aluminous with increasing pressure and can contain a considerably higher Al_2O_3 component than the pyrope composition. In contrast, the MgSiO_3 solubility in corundum decreases with increasing pressure. Additionally, Al_2O_3 incorporation significantly increases the molar volume of bridgmanite, while MgSiO_3 incorporation only slightly increases the volume of corundum. The present study supports the idea that the entire Al_2O_3 content of 4 wt % can be accommodated into bridgmanite in the pyrolytic lower mantle. On the other hand, the Al_2O_3 solubility in

bridgmanite is insufficient to accommodate the entire alumina inventory in subducted slabs in the uppermost part of the lower mantle, owing to the low temperatures and limited pressures, and additional Al phases may therefore be present at these conditions.

Acknowledgments

We thank T. Kawazoe and D. Druzhbin for their assistances at SPring-8 and D. Krauß for his technical assistance in electron microprobe analysis. We also thank Y. Kojima for his help with the focused ion beam system to prepare TEM sample foils. The manuscript is greatly improved by the constructive comments of R. G. Trønnes and an anonymous reviewer and the editorial handling by M. Walter. In situ X-ray diffraction measurements were conducted at SPring-8 (proposal 2015A1359, 2015B1196, 2016A1434, 2016A1172, 2016A1274, and 2016B1094), and some high-pressure cell parts are made in Geodynamics Research Center and supported by PRIUS of Ehime University. All the data are available in the tables and figures in the main text and supporting information. A more detailed discussion of the methodology can be found in the supporting information (Liu et al., 2016; Shcheka et al., 2006; Tange et al., 2009; Van Cappellen & Doukhan, 1994). The Focused Ion Beam instrument (FEI, Scios DualBeam) at Bayerisches Geoinstitut was financed by a DFG grant INST 91/315-1 FUGG. Z. L. was financially supported by the Bayerisches Geoinstitut Visitor's Program. This study was also supported by research grants to T. K. (BMBF: 05K13WC2 and 05K13WC2 and DFG: KA3434/3-1, KA3434/7-1, KA3434/8-1, and KA3434/9-1).

References

- Akaogi, M., Tanaka, A., & Ito, E. (2002). Garnet-ilmenite-perovskite transitions in the system $\text{Mg}_3\text{Si}_2\text{O}_7\text{-Mg}_3\text{Al}_2\text{Si}_2\text{O}_{12}$ at high pressures and high temperatures: Phase equilibria, calorimetry and implications for mantle structure. *Physics of the Earth and Planetary Interiors*, 132(4), 303–324. [https://doi.org/10.1016/S0031-9201\(02\)00075-4](https://doi.org/10.1016/S0031-9201(02)00075-4)
- Andrault, D., Bolfan-Casanova, N., Bouhifd, M., Guignot, N., & Kawamoto, T. (2007). The role of Al-defects on the equation of state of Al-(Mg, Fe)SiO₃ perovskite. *Earth and Planetary Science Letters*, 263(3–4), 167–179. <https://doi.org/10.1016/j.epsl.2007.08.012>
- Brodholt, J. P. (2000). Pressure-induced changes in the compression mechanism of aluminous perovskite in the Earth's mantle. *Nature*, 407(6804), 620–622. <https://doi.org/10.1038/35036565>
- D'Amour, H., Schiferl, D., Denner, W., Schulz, H., & Holzapfel, W. B. (1978). High-pressure single-crystal structure determinations for ruby up to 90 kbar using an automatic diffractometer $P = 0$ kbar. *Journal of Applied Physics*, 49(8), 4411–4416. <https://doi.org/10.1063/1.325494>
- Fei, Y., Wang, Y., & Finger, L. W. (1996). Maximum solubility of FeO in (Mg,Fe)SiO₃ perovskite as a function of temperature at 26 GPa: Implication for the FeO content in the lower mantle. *Journal of Geophysical Research*, 101(B5), 11,525–11,530. <https://doi.org/10.1029/96JB00408>
- Funamori, N., Yagi, T., Miyajima, N., & Fujino, K. (1997). Transformation in garnet: From orthorhombic perovskite to LiNbO₃ phase on release of pressure. *Science*, 275(5299), 513–515. <https://doi.org/10.1126/science.275.5299.513>
- Green, D. H., Hibberson, W. O., & Jaques, A. L. (1979). Petrogenesis of mid-ocean ridge basalts. In M. W. McElhinny (Ed.), *The Earth: Its Origin, Structure and Evolution* (pp. 269–299). London: Academic Press.
- Hirose, K., & Fei, Y. (2002). Subsolidus and melting phase relations of basaltic composition in the uppermost lower mantle. *Geochimica et Cosmochimica Acta*, 66(12), 2099–2108. [https://doi.org/10.1016/S0016-7037\(02\)00847-5](https://doi.org/10.1016/S0016-7037(02)00847-5)
- Hirose, K., Fei, Y., Yagi, T., & Funakoshi, K. (2001). In situ measurements of the phase transition boundary in $\text{Mg}_3\text{Al}_2\text{Si}_2\text{O}_{12}$: Implications for the nature of the seismic discontinuities in the Earth's mantle. *Earth and Planetary Science Letters*, 184(3–4), 567–573. [https://doi.org/10.1016/S0012-821X\(00\)00354-X](https://doi.org/10.1016/S0012-821X(00)00354-X)
- Hirsch, L. M., & Shankland, T. J. (1991). Point defects in silicate perovskite. *Geophysical Research Letters*, 18(7), 1305–1308. <https://doi.org/10.1029/91GL01582>
- Irfune, T. (1987). An experimental investigation of the pyroxene-garnet transformation in a pyrolite composition and its bearing on the constitution of the mantle. *Physics of the Earth and Planetary Interiors*, 45(4), 324–336. [https://doi.org/10.1016/0031-9201\(87\)90040-9](https://doi.org/10.1016/0031-9201(87)90040-9)
- Irfune, T. (1994). Absence of an aluminous phase in the upper part of the Earth's lower mantle. *Nature*, 370(6485), 131–133. <https://doi.org/10.1038/370131a0>
- Irfune, T., & Ringwood, A. E. (1993). Phase transformations in subducted oceanic crust and buoyancy relationships at depths of 600–800 km in the mantle. *Earth and Planetary Science Letters*, 117(1–2), 101–110. [https://doi.org/10.1016/0012-821X\(93\)90120-X](https://doi.org/10.1016/0012-821X(93)90120-X)
- Irfune, T., & Tsuchiya, T. (2007). Phase transition and mineralogy of the lower mantle. In G. D. Price (Ed.), *Treatise on Geophysics* (Vol. 2, pp. 33–62). Amsterdam: Elsevier. <https://doi.org/10.1016/B978-0-444-52748-6.00030-4>
- Irfune, T., Fujino, K., & Ohtani, E. (1991). A new high-pressure form of MgAl_2O_4 . *Nature*, 349(6308), 409–411. <https://doi.org/10.1038/349409a0>
- Irfune, T., Koizumi, T., & Ando, J. (1996). An experimental study of the garnet-perovskite transformation in the system $\text{MgSiO}_3\text{-Mg}_3\text{Al}_2\text{Si}_2\text{O}_{12}$. *Physics of the Earth and Planetary Interiors*, 96(2–3), 147–157. [https://doi.org/10.1016/0031-9201\(96\)03147-0](https://doi.org/10.1016/0031-9201(96)03147-0)
- Ishii, T., Shi, L., Huang, R., Tsujino, N., Druzhbin, D., Myhill, R., ... Katsura, T. (2016). Generation of pressure over 40 GPa using Kawai-type multi-anvil press with tungsten carbide anvils. *The Review of Scientific Instruments*, 87, 024501–1–024501–6(2), 024501. <https://doi.org/10.1063/1.4941716>
- Ishii, T., Sinmyo, R., Komabayashi, T., Boffa-Ballaran, T., Kawazoe, T., Miyajima, N., ... Katsura, T. (2017). Synthesis and crystal structure of LiNbO₃-type $\text{Mg}_3\text{Al}_2\text{Si}_2\text{O}_{12}$: A possible indicator of shock conditions of meteorites. *American Mineralogist*, 102(9), 1947–1952. <https://doi.org/10.2138/am-2017-6027>
- Ito, E., & Matsui, Y. (1978). Synthesis and crystal-chemical characterization of MgSiO_3 perovskite. *Earth and Planetary Science Letters*, 38(2), 443–450. [https://doi.org/10.1016/0012-821X\(78\)90119-X](https://doi.org/10.1016/0012-821X(78)90119-X)
- Ito, E., Kubo, A., Katsura, T., Akaogi, M., & Fujita, T. (1998). High-pressure transformation of pyrope ($\text{Mg}_3\text{Al}_2\text{Si}_2\text{O}_{12}$) in a sintered diamond cubic anvil assembly. *Geophysical Research Letters*, 25(6), 821–824. <https://doi.org/10.1029/98GL00519>
- Katsura, T., Funakoshi, K., Kubo, A., Nishiyama, N., Tange, Y., Sueda, Y., ... Utsumi, W. (2004). A large-volume high-pressure and high-temperature apparatus for in situ X-ray observation, SPEED-Mk.II. *Physics of the Earth and Planetary Interiors*, 143–144, 497–506.
- Katsura, T., Yoneda, A., Yamazaki, D., Yoshino, T., & Ito, E. (2010). Adiabatic temperature profile in the mantle. *Physics of the Earth and Planetary Interiors*, 183(1–2), 212–218. <https://doi.org/10.1016/j.pepi.2010.07.001>
- Keppler, H., & Frost, D. J. (2005). Introduction to minerals under extreme conditions. In R. Miletich (Ed.), *EMU Notes in Mineralogy* (Vol. 7, pp. 1–30). Budapest: Eötvös University Press.
- Kesson, S. E., Fitzgerald, J. D., Shelley, J. M. G., & Withers, R. L. (1995). Phase relations, structure and crystal chemistry of some aluminous perovskites. *Earth and Planetary Science Letters*, 134(1–2), 187–201. [https://doi.org/10.1016/0012-821X\(95\)00112-P](https://doi.org/10.1016/0012-821X(95)00112-P)
- Kirby, S. H., Stein, S., Okal, E. A., & Rubie, D. C. (1996). Metastable mantle phase transformations and deep earthquakes in subducting oceanic lithosphere. *Reviews of Geophysics*, 34(2), 261–306. <https://doi.org/10.1029/96RG01050>
- Kröger, F. A., & Vink, H. H. (1956). Relations between the concentrations of imperfections in crystalline solids. *Solid State Physics*, 3, 307–435. [https://doi.org/10.1016/S0081-1947\(08\)60135-6](https://doi.org/10.1016/S0081-1947(08)60135-6)
- Kubo, A., & Akaogi, M. (2000). Post-garnet transitions in the system $\text{Mg}_3\text{Si}_2\text{O}_7\text{-Mg}_3\text{Al}_2\text{Si}_2\text{O}_{12}$ up to 28 GPa: Phase relations of garnet, ilmenite and perovskite. *Physics of the Earth and Planetary Interiors*, 121(1–2), 85–102. [https://doi.org/10.1016/S0031-9201\(00\)00162-X](https://doi.org/10.1016/S0031-9201(00)00162-X)
- Litasov, K. D., & Ohtani, E. (2005). Phase relations in hydrous MORB at 18–28 GPa: Implications for heterogeneity of the lower mantle. *Physics of the Earth and Planetary Interiors*, 150(4), 239–263. <https://doi.org/10.1016/j.pepi.2004.10.010>
- Liu, Z. D., Irfune, T., Nishi, M., Tange, Y., Arimoto, T., & Shinmei, T. (2016). Phase relations in the system $\text{MgSiO}_3\text{-Al}_2\text{O}_3$ up to 52 GPa and 2000 K. *Physics of the Earth and Planetary Interiors*, 257, 18–27. <https://doi.org/10.1016/j.pepi.2016.05.006>
- McCammon, C. A. (1997). Perovskite as a possible sink for ferric iron in the lower mantle. *Nature*, 387(6634), 694–696. <https://doi.org/10.1038/42685>

- McDonough, W. F., & Sun, S.-S. (1995). The composition of the Earth. *Chemical Geology*, 120(3–4), 223–253. [https://doi.org/10.1016/0009-2541\(94\)00140-4](https://doi.org/10.1016/0009-2541(94)00140-4)
- Miyajima, N., Fujino, K., Funamori, N., Kondo, T., & Yagi, T. (1999). Garnet-perovskite transformation under conditions of the Earth's lower mantle: An analytical transmission electron microscopy study. *Physics of the Earth and Planetary Interiors*, 116(1–4), 117–131. [https://doi.org/10.1016/S0031-9201\(99\)00127-2](https://doi.org/10.1016/S0031-9201(99)00127-2)
- Miyajima, N., Yagi, T., Hirose, K., Kondo, T., Fujino, K., & Miura, H. (2001). Potential host phase of aluminium and potassium in the Earth's lower mantle. *American Mineralogist*, 86(5–6), 740–746. <https://doi.org/10.2138/am-2001-5-614>
- Navrotsky, A. (1999). A lesson from ceramics. *Science*, 284, 1788–1789.
- Navrotsky, A., Schoenitz, M., Kojitani, H., Xu, H., Zhang, J., Weidner, D. J., & Jeanloz, R. (2003). Aluminum in magnesium silicate perovskite: Formation, structure, and energetics of magnesium-rich defect solid solutions. *Journal of Geophysical Research*, 108(B7), 2330.
- Nishio-Hamane, D., Nagai, T., Fujino, K., Seto, Y., & Takafuji, N. (2005). Fe³⁺ and Al solubilities in MgSiO₃ perovskite: Implication of the Fe³⁺/AlO₃ substitution in MgSiO₃ perovskite at the lower mantle condition. *Geophysical Research Letters*, 32(16), L16306. <https://doi.org/10.1029/2005GL023529>
- Ono, S., Ito, E., & Katsura, T. (2001). Mineralogy of subducted basaltic crust (MORB) from 25 to 37 GPa, and chemical heterogeneity of the lower mantle. *Earth and Planetary Science Letters*, 190(1–2), 57–63. [https://doi.org/10.1016/S0012-821X\(01\)00375-2](https://doi.org/10.1016/S0012-821X(01)00375-2)
- Panero, W. R., Akber-Knutson, S., & Stixrude, L. (2006). Al₂O₃ incorporation in MgSiO₃ perovskite and ilmenite. *Earth and Planetary Science Letters*, 252(1–2), 152–161. <https://doi.org/10.1016/j.epsl.2006.09.036>
- Richmond, N. C., & Brodholt, J. P. (1998). Calculated role of aluminum in the incorporation of ferric iron into magnesium silicate perovskite. *American Mineralogist*, 83(9–10), 947–951. <https://doi.org/10.2138/am-1998-9-1003>
- Ringwood, A. E. (1967). The pyroxene-garnet transformation in the Earth's mantle. *Earth and Planetary Science Letters*, 2(3), 255–263. [https://doi.org/10.1016/0012-821X\(67\)90138-0](https://doi.org/10.1016/0012-821X(67)90138-0)
- Ringwood, A. E. (1975). *Composition and petrology of the Earth's mantle*. New York: McGraw-Hill.
- Ringwood, A. E. (1991). Phase transformations and their bearing on the constitution and dynamics of the mantle. *Geochimica et Cosmochimica Acta*, 55(8), 2083–2110. [https://doi.org/10.1016/0016-7037\(91\)90090-R](https://doi.org/10.1016/0016-7037(91)90090-R)
- Shcheka, S. S., Wiedenbeck, M., Frost, D. J., & Keppler, H. (2006). Carbon solubility in mantle minerals. *Earth and Planetary Science Letters*, 245(3–4), 730–742. <https://doi.org/10.1016/j.epsl.2006.03.036>
- Stebbins, J. F., Kroeker, S., & Andraut, D. (2001). The mechanism of solution of aluminum oxide in MgSiO₃ perovskite. *Geophysical Research Letters*, 28(4), 615–618. <https://doi.org/10.1029/2000GL012279>
- Sun, S. (1982). Chemical composition and the origin of the Earth's primitive mantle. *Geochimica et Cosmochimica Acta*, 46(2), 179–192. [https://doi.org/10.1016/0016-7037\(82\)90245-9](https://doi.org/10.1016/0016-7037(82)90245-9)
- Tange, Y., Irifune, T., & Funakoshi, K. (2008). Pressure generation to 80 GPa using multianvil apparatus with sintered diamond anvils. *High Pressure Research*, 28(3), 245–254. <https://doi.org/10.1080/08957950802208936>
- Tange, Y., Takahashi, E., Nishihara, Y., Funakoshi, K., & Sata, N. (2009). Phase relations in the system MgO-FeO-SiO₂ to 50 GPa and 2000°C: An application of experimental techniques using multianvil apparatus with sintered diamond anvils. *Journal of Geophysical Research*, 114(B2), B02214. <https://doi.org/10.1029/2008JB005891>
- Tsuchiya, T. (2003). First-principles prediction of the P-V-T equation of state of gold and the 660-km discontinuity in Earth's mantle. *Journal of Geophysical Research*, 108, B10.
- Van Cappellen, V., & Doukhan, J. C. (1994). Quantitative transmission X-ray microanalysis of ionic compounds. *Ultramicroscopy*, 53(4), 343–349. [https://doi.org/10.1016/0304-3991\(94\)90047-7](https://doi.org/10.1016/0304-3991(94)90047-7)
- Walter, M., Kubo, A., Yoshino, T., Brodholt, J., Koga, K. T., & Ohishi, Y. (2004). Phase relations and equation-of-state of aluminous Mg-silicate perovskite and implications for Earth's lower mantle. *Earth and Planetary Science Letters*, 222(2), 501–516. <https://doi.org/10.1016/j.epsl.2004.03.014>
- Walter, M., Trønnes, R. G., Armstrong, L. S., Lord, O., Caldwell, W. A., & Clark, A. M. (2006). Subsolidus phase relations and perovskite compressibility in the system MgO-AlO_{1.5}-SiO₂ with implications for Earth's lower mantle. *Earth and Planetary Science Letters*, 248(1–2), 77–89. <https://doi.org/10.1016/j.epsl.2006.05.017>
- Weng, K., Mao, H. K., & Bell, P. M. (1981). *Lattice parameters of the perovskite phase in the system MgSiO₃-CaSiO₃-Al₂O₃*. *Carnegie Inst* (Vol. 81, pp. 273–277). Washington: Year Book.
- Xu, Y., McCammon, C. A., & Poe, B. T. (1998). The effect of alumina on the electrical conductivity of silicate perovskite. *Science*, 282(5390), 922–924. <https://doi.org/10.1126/science.282.5390.922>
- Yagi, T., Okabe, K., Nishiyama, N., Kubo, A., & Kikegawa, T. (2004). Complicated effects of aluminum on the compressibility of silicate perovskite. *Physics of the Earth and Planetary Interiors*, 143–144, 81–89.
- Zhang, J., & Weidner, D. J. (1999). Thermal equation of state of aluminium-enriched silicate perovskite. *Science*, 284(5415), 782–784. <https://doi.org/10.1126/science.284.5415.782>